

Single-Mode Emission in InP Microdisks on Si Using Au Antenna

Preksha Tiwari, Anna Fischer, Markus Scherrer, Daniele Caimi, Heinz Schmid, and Kirsten E. Moselund*

Cite This: *ACS Photonics* 2022, 9, 1218–1225

Read Online

ACCESS |

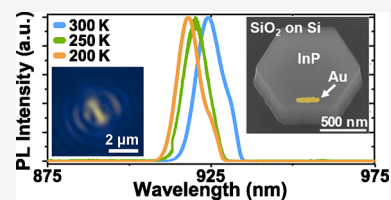
Metrics & More

Article Recommendations

Supporting Information

ABSTRACT: An important building block for on-chip photonic applications is a scaled emitter. Whispering gallery mode cavities based on III–Vs on Si allow for small device footprints and lasing with low thresholds. However, multimodal emission and wavelength stability over a wider range of temperature can be challenging. Here, we explore the use of Au nanorod antennae on InP whispering gallery mode lasers on Si for single-mode emission. We show that by proper choice of the antenna size and positioning, we can suppress the side modes of a cavity and achieve single-mode emission over a wide excitation range. We establish emission trends by varying the size of the antenna and show that the far-field radiation pattern differs significantly for devices with and without antenna. Furthermore, the antenna-induced single-mode emission is dominant from room temperature (300 K) down to 200 K, whereas the cavity without an antenna is multimodal and its dominant emission wavelength is highly temperature-dependent.

KEYWORDS: laser, nanoantenna, whispering gallery mode, cavity, photonics, plasmonics



INTRODUCTION

Integrated light sources show potential for a wide range of applications, from optical communication to quantum information processing to sensing. Using Si as a material platform allows to leverage established fabrication processes for passive structures. Due to its indirect band gap, however, an alternative material is needed for active devices. Group III–V semiconductors pose a viable choice for emitters^{1–5} and detectors^{6–11} due to their direct and tuneable band gap, high mobilities, and high absorption coefficients covering the entire telecommunication band.

Small mode volumes and low thresholds can be achieved by various cavity types, like photonic crystal cavities,^{12–17} metal-clad cavities,^{18–23} semiconductor-on-metal cavities,^{24,25} or whispering gallery mode (WGM) microdisk cavities,^{26–29} based on total internal reflection. The latter have the advantage of possessing a simple fabrication scheme. However, mode selectivity and multimodal emission can be a challenge, which will be addressed in the present work. Furthermore, a general challenge in III–V semiconductors photonics is their strong temperature sensitivity: the band gap follows the Varshni shift,³⁰ leading to a change in spectral overlap between the material gain and resonant mode wavelengths at different temperatures.

Single-mode emission can be achieved by suppressing the side modes and breaking the symmetry of the devices: One way to achieve single-mode lasing in microdisk cavities was demonstrated using suspended cavities with a proper choice of bridges manipulating the spatial symmetry.³¹ Another strategy involves using grooves³² or nanoantennae.^{33,34} Recently, nanoantennae have also been combined with high-Q cavities containing quantum dots, leading to hybrid systems where

emission enhancements exceed those of a bare cavity and allow for tuning the bandwidth.^{35,36} These demonstrations show the strong potential of nanoantennae for single-photon devices³⁷ and toward strongly coupled systems.³⁸ For plasmonic nanoantennae, it has been shown that, following the Mie–Gans scattering, the scattering cross sections in the visible and near infrared, as well as resonances, are tunable and dependent on the aspect ratio of the antennae.^{39–41} This enables optimization of antenna geometry to enhance or suppress emission of a specific wavelength range.

While side-mode suppression and enhanced directivity were successfully demonstrated for microdisk cavities coupled with a Pt antenna without degradation of the dominant mode in terms of threshold,³³ the impact of the metallic antenna and its geometry on wavelength stability, also considering different temperatures, remains to be studied. Here, we explore the effect of Au nanorod antennae on top of InP microdisk lasers fabricated on Si. Using a relatively simple process based on direct wafer bonding, etching, and lift-off, we are able to fabricate a large number of devices. This allows us to get insight into general trends of the antenna size and position on the resonant emission of the WGM cavities. We observe significantly improved device performance in terms of side-mode suppression and wavelength stability for different

Received: October 31, 2021

Published: March 17, 2022



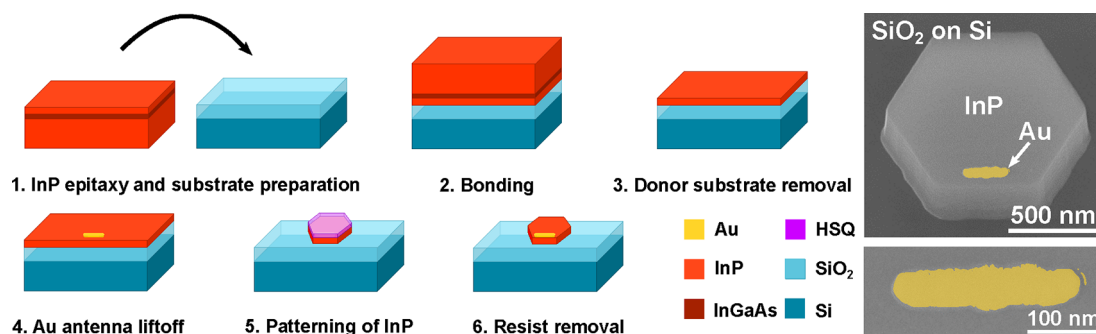


Figure 1. Illustration of the fabrication steps. After wafer bonding, the Au antennae are defined via lift-off. The InP microdisk cavities are etched afterward, and the top HSQ resist is removed. The SEM image shows a device with a parallel antenna and a zoom-in of the Au nanorod (false-colored).

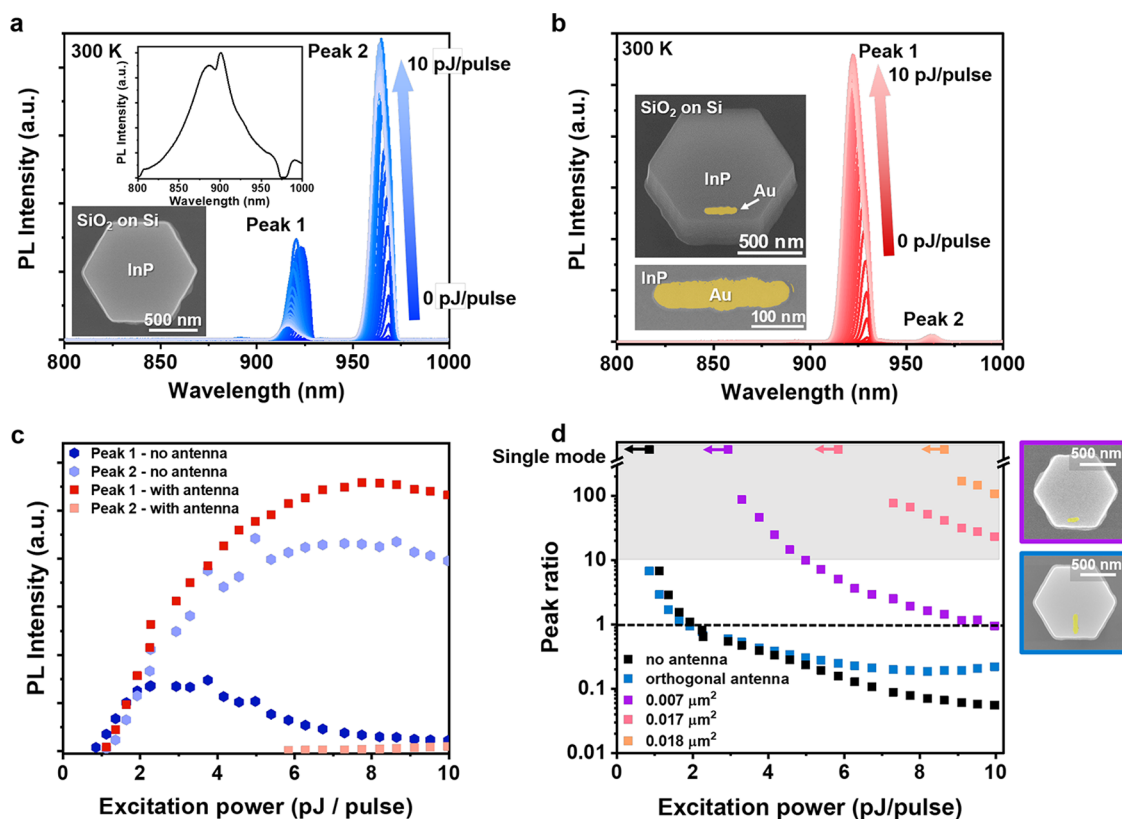


Figure 2. (a) Bulk emission (inset) and emission spectrum upon increasing excitation energy for a 1100 nm wide and 225 nm thick InP cavity bonded on Si. (b) Emission spectrum for a 1100 nm wide InP cavity with a parallel antenna on top. (c) LL curve for the spectrum shown in (a,b) from which the threshold is extracted. (d) Peak ratio of peak 1 at 925 nm and peak 2 at 960 nm for a bare cavity and antenna with varying sizes and orientations. The shaded part highlights the region where the peak ratio is greater than 10. The points with arrows pointing toward the “single mode” label mark the excitation powers, up to which a certain device is single mode, that is, where only one resonant emission peak is visible. Corresponding SEM images for the orthogonal antenna and the parallel antenna with an area of $0.007 \mu\text{m}^2$ are shown on the right.

temperatures. We believe that these findings are of general interest for the optimization of the emission characteristics of micro- and nanolasers.

RESULTS AND DISCUSSION

Device Fabrication. A 225 nm thick InP layer is grown on a lattice-matched sacrificial InP wafer with an InGaAs etch stop layer in between using metal–organic chemical vapor deposition. Then, the material is bonded onto a Si wafer with a $2 \mu\text{m}$ thick SiO_2 layer in between, serving as an optical insulator layer, and the donor wafer material is removed. More information on direct wafer-bonding techniques can be found

in ref 42. For the microdisk cavities, the antennae are first defined by a lift-off process using a PMMA bilayer as a resist and 40 nm electron-beam evaporated Au and a 2 nm Ti adhesion layer. Hexagonal microdisks are then patterned using HSQ as a resist. InP microdisks with a width of 1100 nm and a thickness of 225 nm are etched by inductively coupled plasma dry etching using CH_4 , Cl_2 , and H_2 . After the etch, the sample is cleaned with a 1:10 diluted phosphoric acid solution and capped with 3 nm of Al_2O_3 using atomic layer deposition. The antennae are 40–70 nm wide and 150–300 nm long and are either placed along (parallel) the side facet of the InP cavity or rotated in-plane by 90° (orthogonal) with respect to it. The

distance between the antenna and the cavity edge is designed to be 50 nm but varies due to drift and alignment accuracy during the patterning process or nonoptimal adhesion. Figure 1 illustrates the fabrication steps and shows a scanning electron microscopy (SEM) image of the final device with a parallelly placed antenna.

All measurements are performed with a micro-photoluminescence (micro-PL) setup where a ps-pulsed excitation source with emission at 750 nm and a repetition rate of 78 MHz is focused onto the device with a 100 \times objective (NA = 0.6) and a spot-size of approximately 1 μ m. The emitted PL is collected in reflection mode from the top of the device, and the spectrum is detected by a linear array InGaAs detector. In the following, we will discuss the impact on the emission spectrum of the microdisk through the use of Au antennae with varying cross-sectional areas. In some cases, the different antenna widths will be additionally color coded in the figures in order to map them to respective cross-section areas.

Comparison of Different Orientations. Figure 2a shows the PL emission spectra of a 1.1 μ m wide device without antenna upon increasing input power with the bulk emission of InP in the inset. Two resonant emission peaks at around 925 nm (peak 1) and 960 nm (peak 2) emerge at higher excitation energies. Figure 2b shows the emission spectra upon increasing input power for a cavity with a parallelly oriented Au antenna on top. Compared to the bare cavity case, peak 2 is suppressed.

The light-in-light-out (LL) curve in Figure 2c shows a multimode behavior with similar thresholds for peaks 1 and 2 in the bare cavity case, which are 0.8 and 1.2 pJ/pulse, respectively. For the antenna-coupled cavity, the threshold of peak 1 is 1.1 pJ/pulse and its intensity is slightly higher than peak 2 of the bare cavity, but the latter is most likely a result of the stronger emission of InP at a wavelength of 925 nm compared to 960 nm. Peak 2 of this device, however, is significantly suppressed and only appears at higher powers, whereas at pump powers below \sim 6 pJ/pulse, the antenna-coupled device is single mode, that is, no second resonant wavelength peak is visible.

From LL curves like the one in Figure 2c, peak ratios between peak 1 and peak 2 are determined and illustrated in Figure 2d for the bare cavity and four different cavities with antennae of varying dimensions and positions: for the bare cavity, peak 1 is the dominant peak at first; then the ratio between the amplitude of the two peaks rapidly decreases and the longer-wavelength peak 2 dominates after around 2 pJ/pulse, indicated by a peak ratio value <1 . On the other hand, for the parallelly oriented antennae, peak 1 stays dominant for the larger antennae over the entire excitation range. Only the small antenna with a cross section of 0.007 μ m² has a crossover at around 10 pJ/pulse. Also, it is notable that the antenna-coupled devices are single mode for lower excitation powers, and the slight multimode behavior only appears for increasingly higher powers as the size of the antenna is decreased.

For the orthogonally placed antenna, the multimode behavior is similar to the bare cavity, and there is no side-mode suppression effect. Only at higher excitation powers does the peak ratio deviate, potentially due to mode competition and other effects in the cavity. More peak ratios for orthogonally placed antennae are shown in Figure S1 in the Supporting Information, detailing that unlike for the parallelly placed antennae, larger cross sections do not affect the side-mode suppression. The low selectivity of the orthogonally

placed antenna can potentially be attributed to the lower overlap of the resonant mode, the polarization of the mode, and the scattering cross section of the antenna: the WGM is expected to be at the periphery of the cavity; hence, an orthogonally placed antenna may overlap with a node of the mode or only partially if not placed accurately. For the parallelly placed nanoantenna, exact positioning may be less crucial because a larger fraction of the antenna is expected to overlap with the electric field.

To illustrate this concept, we performed 3D finite difference time domain (FDTD) simulations to analyze the mode pattern of a bare cavity and a cavity with parallelly and orthogonally placed antennae using the commercial software Lumerical. We have added these data to the Supporting Information since they give insight into the importance of the antenna positioning with respect to the field distribution of the resonant mode. Nevertheless, we want to point out that the challenge with these simulations is that the microdisks support multiple modes and the fabricated devices may emit in another mode than the simulated one due to processing imperfections.

Figure 3a shows the emission spectra for a bare cavity, a device with an orthogonal antenna, and a device with a parallel

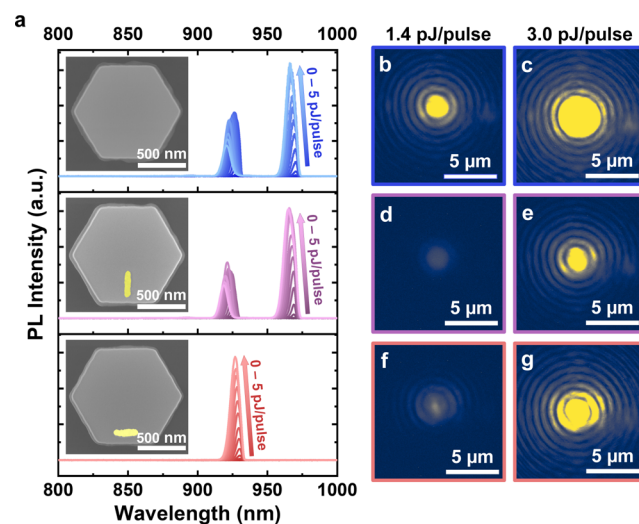


Figure 3. (a) Room-temperature emission spectrum upon increasing excitation energy (0–5 pJ/pulse) for a 1100 nm wide and 225 nm thick InP cavity bonded on Si, without antenna (first row, blue), with an orthogonal antenna (second row, purple), and with a parallel antenna (red, third row). Inset: SEM images of the characterized devices. Far-field radiation images with first-order interference patterns for the devices shown in (a) at 1.4 pJ/pulse (b,d,f) and 3 pJ/pulse (c,e,g). (b,c) correspond to the bare cavity, (d,e) correspond to the device with an orthogonal antenna, and (f,g) correspond to the device with a parallel antenna.

antenna (see inset SEM images for the devices): in accordance with the results presented in Figures 2 and S1 of the Supporting Information, the side mode is only suppressed for the device with the parallel antenna. Far-field radiation images of these devices captured at 1.4 and 3 pJ/pulse are shown in Figure 3b–g. Below the threshold, a faint emission without any interference patterns is recorded (see Figure 3d for the case of a device with an orthogonal antenna but representative for all types of devices below the threshold). Above the threshold, first-order interference patterns, which are evidence of lasing, can be seen in the far-field image as shown in Figure 3b,c,e–g.

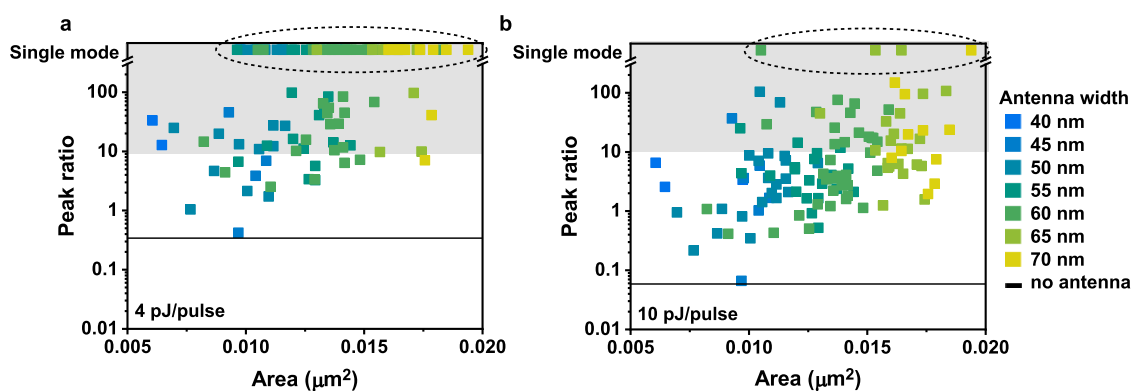


Figure 4. Peak ratio (PL intensity peak 1/PL intensity peak 2) for all measured devices vs antenna area at an excitation power of (a) 4 and (b) 10 pJ/pulse. The circled devices were single mode (only one resonant emission peak visible). The shaded area corresponds to peak ratios which are higher than 10.

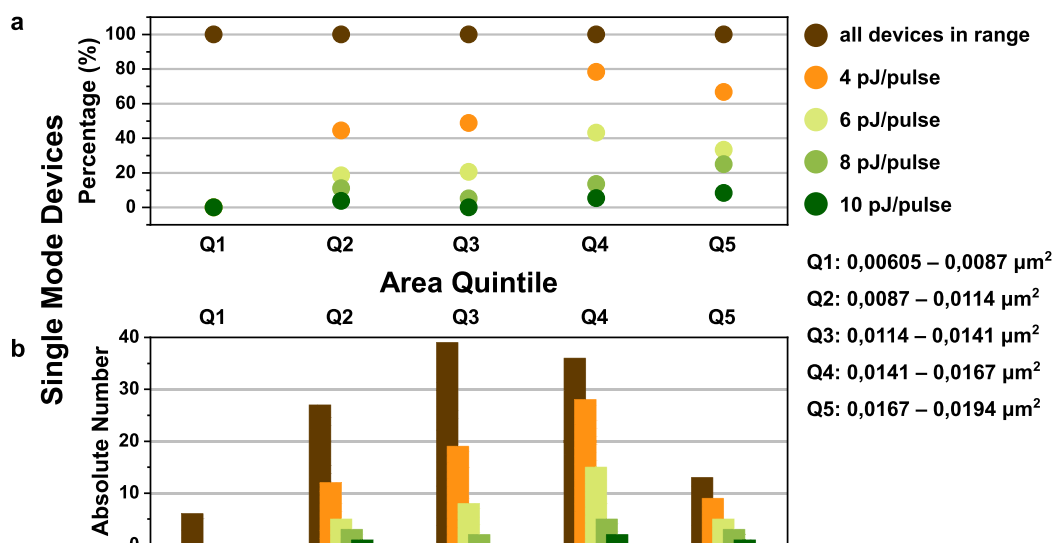


Figure 5. Single-mode devices binned into areas of smallest to largest quintile (a) in percentage and (b) in absolute numbers.

While the far-field has a circular shape for the bare cavity case, it is asymmetric for the devices with an antenna. This suggests that the antenna acts as a scattering element, irrespective of its orientation, and thus alters the detected far-field radiation profile. In order to gain more insight into the spatial distribution of the scattered light, k-space measurements would be desirable. Unfortunately, this capability is not available in our setup.

Selectivity for Different Antenna Areas. In total, 121 devices with parallelly placed antennae covering areas from 0.00605 to 0.0194 μm^2 were measured, and the following results shall be representative of general trends. Figure 4 shows the peak ratio versus the antenna cross-section area at 4 and 10 pJ/pulse for all measured devices. The peak ratios are additionally color coded corresponding to the different antenna widths for clearer visualization. If only one emission peak is visible, we refer to the devices as single mode. We define peak 1 to be dominating if the peak ratio rises over 10. When the peak ratio is below 1, this means that peak 2 is the dominant peak. This is the case for cavities without antenna (see solid line in Figure 4 which corresponds to peak ratio values for the bare cavity) or for some of the smallest antennae sizes, especially at higher excitation energies. In general, antenna-coupled devices show a higher peak ratio value with a

more dominant emission of peak 1 for the entire excitation range. Some cavities even exhibit single-mode emission up to 10 pJ/pulse. Furthermore, the larger antennae tend to be more selective than the smaller ones with higher peak ratios and more single-mode devices. The overall spread in the peak ratio for a certain antenna area can be explained by fabrication-related deviations of the antenna shape (varying width across the structure) and positioning (slight tilt and different edge-to-antenna spacing due to adhesion and drift during processing).

To quantify this trend further, the devices were binned into quintiles ranging from the smallest (Q1) to largest (Q5) device areas, and the number of single-mode devices at different powers were determined. Figure 5a shows the percentage of measured devices which were single mode at 4, 6, 8, and 10 pJ/pulse. Figure 5b shows the absolute number of measured and single-mode devices corresponding to the percentage shown in Figure 5a. As in Figure 4, a trend is visible toward larger antenna areas: while in the smallest quintile, no device was single mode, in the largest two, there are 80% and almost 70%, respectively. At 10 pJ/pulse only four of the measured devices are single mode, and three of those are in the largest two quintiles. It seems that the most selective antennae were in bin Q4, corresponding to the second largest quintile with areas ranging from 0.0141 to 0.0167 μm^2 . It should be noted,

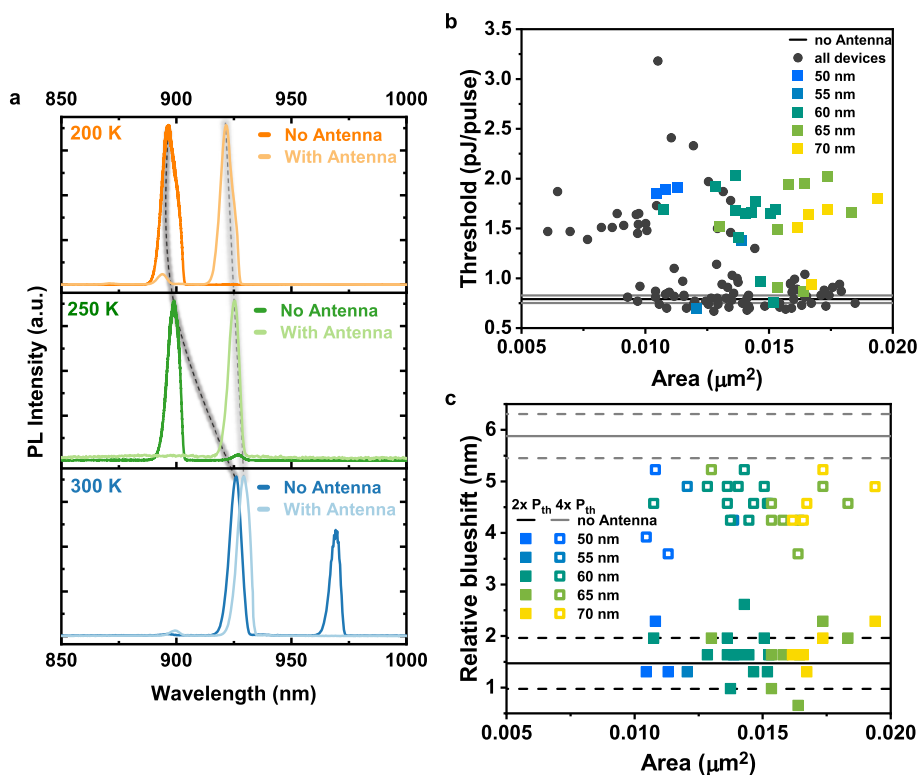


Figure 6. (a) Spectrum for devices with (light colors) and without antenna (dark colors) at different temperatures. The dark dashed line outlines the change of the dominant emission mode for the bare cavity, and the light dashed line tracks the peak position for the antenna-coupled devices. (b) Threshold of the bare cavity (solid black line for average of 10 devices and gray line indicating the standard deviation) and antenna-coupled devices vs antenna area. The square, colored points correspond to devices which are single mode up to 6 pJ/pulse or more, and the gray points correspond to all antenna devices which were measured. (c) Relative peak shift for devices which were single mode up to 6 pJ/pulse or more at $2\times$ (solid points) and $4\times$ (hollow points) the threshold. The solid line corresponds to the average blue shift of 10 bare cavities (around 1.5 nm at $2\times$ threshold and almost 6 nm at $4\times$ threshold power). The dashed line shows the standard deviation of the blue shift for the bare cavities.

however, that for Q5, the total number of measured devices is lower than that for Q4 (12 vs 35 devices), so a less selective antenna will weigh heavier in the percentage.

These results may be taken as an indication that there is a certain optimum in terms of antenna size: initially, an increase in the antenna size will provide improved side-mode suppression, whereas eventually this effect saturates. It is expected that several effects might impact the mode selectivity and device performance: the scattering and absorption at a certain wavelength depend on the antenna area and substrate.^{39,40,43,44} So, depending on the antenna size and position, one resonant mode may be influenced stronger than the other, or both modes might be affected similarly.

Performance at Different Temperatures. To investigate the extent to which the antenna not only allows for side-mode suppression but also wavelength stability, we performed micro-PL measurements at various temperatures. Since the band gap of InP is temperature-dependent, the gain emission peak shifts to lower wavelengths upon temperature decrease, leading to a change of the dominant resonant mode to the one which now has a stronger overlap with the bulk PL. In the antenna-coupled case, however, the dominant resonant wavelength stays the same down to 200 K, and the mode at 900 nm is suppressed, as it is shown in Figure 6a. This indicates that the antenna is not merely preferentially scattering a particular wavelength but that it enhances either the dominant mode or suppresses the others and thereby counterbalances the temperature-dependent shift of the gain. This is a significant result as

temperature stabilization in nanophotonic components is a great challenge.

When placing a metal in close proximity to a resonant cavity, the question naturally arises whether this will lead to an increase in absorption losses and thereby an increase of the threshold for resonant emission. Figure 6b shows the threshold of the different devices versus antenna area for peak 1 at 300 K. The square, colored points correspond to devices which are single mode at least up to 6 pJ/pulse, and the gray points correspond to all antenna-devices which were measured. The threshold of peak 1 is higher for most of the devices which were single mode up to 6 pJ/pulse and comparable to the bare cavity case for most of the other devices. This indicates that the most effective antenna in terms of side-mode suppression leads to a higher threshold, likely due to increased absorption losses associated with the antenna and the optical mode which is directly disturbed by it.

Linear LL curves of the devices at 200 K are shown in Figure S2 in the Supporting Information. The bare cavity has a considerably lower threshold at 200 K (0.3 pJ/pulse) than at room temperature due to enhanced material gain, whereas for the device with the antenna, the threshold (1 pJ/pulse) is insignificantly affected by temperature. One explanation might be the weaker overlap between the gain and the resonant mode competing with the overall enhanced material gain at lower temperatures, and therefore additional energy is needed to compensate for losses.

Table 1. Comparison of Bare Cavities and Selected Antenna-Coupled Devices Which Are Single Mode (Only Peak 1) up to 6 pJ/Pulse^a

	antenna area [μm^2]	threshold P_{th} [pJ/pulse]	blue shift at $2 \times P_{\text{th}}$ [nm]	blue shift at $4 \times P_{\text{th}}$ [nm]	peak ratio at 6 pJ/pulse
bare cavity		0.79 ± 0.04	1.5 ± 0.5	5.9 ± 0.4	0.15 ± 0.05
antenna with the highest side-mode suppression	0.0153	1.49	1.6	4.25	single mode
antenna with the lowest blue shift	0.0164	0.87	0.65	3.6	single mode
antenna with the lowest threshold	0.0121	0.7	1.3	4.9	single mode

^aListed are average threshold, relative blue shift at 2 \times and 4 \times the threshold, and peak ratios at 6 pJ/pulse. For the antenna-coupled devices, the values for the microdisk with the highest side-mode suppression (single mode > 10 pJ/pulse), lowest blue shift, and lowest threshold are given.

Figure 6c shows the relative blue shift of the different devices which were single mode up to 6 pJ/pulse and for the bare cavity case. The blue shift was measured at power levels which corresponded to 2 \times (filled symbols for antenna-coupled devices) and 4 \times (empty symbols for antenna-coupled devices) the threshold. The solid lines correspond to the average blue shift of 10 bare cavities at 2 \times (black) and 4 \times (gray) the threshold. They are around 1.5 nm at 2 \times threshold and almost 6 nm at 4 \times threshold power. The dashed lines show the standard deviation of the blue shift for the bare cavities. The blue shift of the resonant mode upon increasing the input power is related to the plasma dispersion effect,⁴⁵ a change in refractive index caused by the presence of free carriers, and is commonly observed in III–V semiconductor lasers.^{18,26,46} Interestingly, the blue shift at 2 \times the threshold is in a comparable range for the different kinds of devices, but it is larger for the bare cavity case than for the antenna-coupled devices at 4 \times the threshold. This indicates that the antenna effectively clamps the emission wavelength of the resonant mode. This would support the assumption that the mode selectivity may result from a plasmonic effect.

The antenna might reduce the quality factor of the resonant modes since it is expected that additional losses will be introduced to the system. However, we cannot experimentally verify this in our devices since the emission peaks are artificially broadened due to the blue shift discussed above and wavelength chirping in modulated semiconductor lasers. This is commonly observed in other devices from our group¹⁸ as well as in demonstrations of pulsed semiconductor lasers from other groups.^{46–48}

An assessment of the carrier dynamics would be interesting since plasmonics can, for example, be used for high-speed photonics components, such as detectors and modulators.^{49–51} This was unfortunately not possible in the given setup due to the resolution limit of the lifetime measurement setup which is approximately 50 ps. Therefore, we cannot resolve the fast dynamics of this system.

CONCLUSIONS AND OUTLOOK

In this work, we presented a systematic study on the effect of Au nanorod antennae on InP WGM cavities. While the bare InP cavity is multimodal and the dominant resonance wavelength changes significantly with temperature, we show that in antenna-coupled devices, we can achieve single-mode emission and wavelength stability over 100 K (from 200 K up to room temperature at 300 K). The antenna must be aligned properly to the optical mode as we only observed this side-mode suppression for antennae aligned along the cavity periphery (parallel) and not angularly (orthogonal). The beneficial effect of the antennae initially increases with its

relative size until it saturates at dimensions around 0.014–0.017 μm^2 . The antenna reduces the relative blue shift due to the plasma dispersion effect, thereby providing for more stable emission at higher excitation powers. From the combination of these results, we can conclude that the antenna does not just impact light collection via scattering but that the presence of the metal stabilizes the emission mode, thereby improving side-mode suppression and wavelength stability over variations in temperature and pumping powers.

Furthermore, we found that the threshold of the dominant peak is increased in antenna-coupled devices which are single mode up to 6 pJ/pulse, whereas devices which have a lower side-mode suppression are more likely to have similar thresholds compared to the devices without antenna. We attribute absorption losses due to the antenna to be the cause of the higher threshold.

Table 1 summarizes some parameters found in the experiments above. Listed are the average values for the bare cavity and for selected antenna-coupled devices, which were single mode up to 6 pJ/pulse. For the antenna-coupled devices, values corresponding to the device with the overall highest side-mode suppression (single mode at >10 pJ/pulse), the lowest relative blue shift, and the lowest threshold are listed.

We believe the findings to be relevant and portable to a broad range of nanophotonic architectures. A long-term goal would be coupling to more complex laser architectures or exploration of antenna shapes specific to desired emission wavelengths and directions.

ASSOCIATED CONTENT

Supporting Information

The Supporting Information is available free of charge at <https://pubs.acs.org/doi/10.1021/acsp Photonics.1c01677>.

Additional data on selectivity of orthogonal antennae, optical simulations, and emission characteristics at 200 K (PDF)

AUTHOR INFORMATION

Corresponding Author

Kirsten E. Moselund – IBM Research Europe—Zurich, 8803 Rüschlikon, Switzerland; Present Address: Paul-Scherrer Institute (PSI) and EPFL, 5232 Villigen, Switzerland; Email: kirsten.moselund@psi.ch

Authors

Preksha Tiwari – IBM Research Europe—Zurich, 8803 Rüschlikon, Switzerland; orcid.org/0000-0001-5787-2588

Anna Fischer – IBM Research Europe—Zurich, 8803 Rüschlikon, Switzerland; Present Address: Department of

Physics, Imperial College London, Blackett Laboratory, London SW7 2AZ, United Kingdom
Markus Scherrer – IBM Research Europe—Zurich, 8803 Rueschlikon, Switzerland
Daniele Caimi – IBM Research Europe—Zurich, 8803 Rueschlikon, Switzerland
Heinz Schmid – IBM Research Europe—Zurich, 8803 Rueschlikon, Switzerland; orcid.org/0000-0002-0228-4268

Complete contact information is available at:
<https://pubs.acs.org/10.1021/acsp Photonics.1c01677>

Author Contributions

P.T., A.F. and K.M. created the device concept. P.T. fabricated the sample with the support of M.S. and H.S. for material growth, D.C. for the wafer bonding, and A.F. for lift off. A.F. and P.T. performed the optical characterization on the devices. A.F. and P.T. analyzed the data. P.T. performed the FDTD simulations. K.M. led and managed the project. All authors discussed the results. The manuscript was written by P.T. and K.M. with contributions of all authors, and all authors have given approval to the final version of the manuscript.

Funding

The work presented here has received funding from the European Union H2020 ERC Starting Grant project PLASMIC (grant agreement no. 678567) and the European Union H2020 program SEQUENCE (grant no. 871764) and H2020 Marie Skłodowska-Curie Innovative Training Networks project CORAL (grant no. 859841).

Notes

The authors declare no competing financial interest.

ACKNOWLEDGMENTS

The authors gratefully acknowledge Rachel Grange and Andreas Schenk for fruitful technical discussions. We thank the Cleanroom Operations Team of the Binnig and Rohrer Nanotechnology Center (BRNC) for their help and support.

REFERENCES

- (1) Kim, H.; Lee, W.-J.; Farrell, A. C.; Balgarkashi, A.; Huffaker, D. L. Telecom-Wavelength Bottom-up Nanobeam Lasers on Silicon-on-Insulator. *Nano Lett.* **2017**, *17*, 5244–5250.
- (2) Hu, Y.; Liang, D.; Mukherjee, K.; Li, Y.; Zhang, C.; Kurczveil, G.; Huang, X.; Beausoleil, R. G. III/V-on-Si MQW Lasers by Using a Novel Photonic Integration Method of Regrowth on a Bonding Template. *Light Sci. Appl.* **2019**, *8*, 93.
- (3) Chen, R.; Ng, K. W.; Ko, W. S.; Parekh, D.; Lu, F.; Tran, T.-T. D.; Li, K.; Chang-Hasnain, C. Nanophotonic Integrated Circuits from Nanoresonators Grown on Silicon. *Nat. Commun.* **2014**, *5*, 4325.
- (4) Stettner, T.; Thurn, A.; Döblinger, M.; Hill, M. O.; Bissinger, J.; Schmiedeke, P.; Matich, S.; Kostenbader, T.; Ruhstorfer, D.; Riedl, H.; Kaniber, M.; Lauhon, L. J.; Finley, J. J.; Koblmüller, G. Tuning Lasing Emission toward Long Wavelengths in GaAs-(In,Al)GaAs Core–Multishell Nanowires. *Nano Lett.* **2018**, *18*, 6292–6300.
- (5) Schmiedeke, P.; Thurn, A.; Matich, S.; Döblinger, M.; Finley, J. J.; Koblmüller, G. Low-Threshold Strain-Compensated InGaAs/(In,Al)GaAs Multi-Quantum Well Nanowire Lasers Emitting near 1.3 μm at Room Temperature. *Appl. Phys. Lett.* **2021**, *118*, 221103.
- (6) Baumgartner, Y.; Caimi, D.; Sousa, M.; Hopstaken, M.; Salamin, Y.; Baeuerle, B.; Bitachon, B. I.; Leuthold, J.; Faist, J.; Offrein, B. J.; Czornomaz, L. High-Speed CMOS-Compatible III-V on Si Membrane Photodetectors. *Opt. Express* **2021**, *29*, 509.
- (7) Mauthe, S.; Baumgartner, Y.; Sousa, M.; Ding, Q.; Rossell, M. D.; Schenk, A.; Czornomaz, L.; Moselund, K. E. High-Speed III-V

Nanowire Photodetector Monolithically Integrated on Si. *Nat. Commun.* **2020**, *11*, 4565.

(8) Takiguchi, M.; Sasaki, S.; Tatenno, K.; Chen, E.; Nozaki, K.; Sergent, S.; Kuramochi, E.; Zhang, G.; Shinya, A.; Notomi, M. Hybrid Nanowire Photodetector Integrated in a Silicon Photonic Crystal. *ACS Photonics* **2020**, *7*, 3467–3473.

(9) Zhang, J.; De Groote, A.; Abbasi, A.; Loi, R.; O’Callaghan, J.; Corbett, B.; Trindade, A. J.; Bower, C. A.; Roelkens, G. Silicon Photonics Fiber-to-the-Home Transceiver Array Based on Transfer-Printing-Based Integration of III-V Photodetectors. *Opt. Express* **2017**, *25*, 14290.

(10) Wen, P.; Tiwari, P.; Mauthe, S.; Schmid, H.; Sousa, M.; Scherrer, M.; Baumann, M.; Bitachon, B. I.; Leuthold, J.; Gotsmann, B.; Moselund, K. E. Waveguide Coupled III-V Photodiodes Monolithically Integrated on Si. *Nat. Commun.* **2022**, *13*, 909.

(11) Xue, Y.; Han, Y.; Tong, Y.; Yan, Z.; Wang, Y.; Zhang, Z.; Tsang, H. K.; Lau, K. M. High-Performance III-V Photodetectors on a Monolithic InP/SOI Platform. *Optica* **2021**, *8*, 1204.

(12) Scherrer, M.; Vico Triviño, N.; Mauthe, S.; Tiwari, P.; Schmid, H.; Moselund, K. E. In-Plane Monolithic Integration of Scaled III-V Photonic Devices. *Appl. Sci.* **2021**, *11*, 1887.

(13) Mauthe, S.; Tiwari, P.; Scherrer, M.; Caimi, D.; Sousa, M.; Schmid, H.; Moselund, K. E.; Vico Triviño, N. Hybrid III–V Silicon Photonic Crystal Cavity Emitting at Telecom Wavelengths. *Nano Lett.* **2020**, *20*, 8768–8772.

(14) Crosnier, G.; Sanchez, D.; Bouchoule, S.; Monnier, P.; Beaudoin, G.; Sagnes, I.; Raj, R.; Raineri, F. Hybrid Indium Phosphide-on-Silicon Nanolaser Diode. *Nat. Photonics* **2017**, *11*, 297–300.

(15) Takeda, K.; Sato, T.; Fujii, T.; Kuramochi, E.; Notomi, M.; Hasebe, K.; Kakitsuka, T.; Matsuo, S. Heterogeneously Integrated Photonic-Crystal Lasers on Silicon for on/off Chip Optical Interconnects. *Opt. Express* **2015**, *23*, 702.

(16) Zhang, Y.; Khan, M.; Huang, Y.; Ryou, J.; Deotare, P.; Dupuis, R.; Lončar, M. Photonic Crystal Nanobeam Lasers. *Appl. Phys. Lett.* **2010**, *97*, 051104.

(17) Takiguchi, M.; Yokoo, A.; Nozaki, K.; Birowosuto, M. D.; Tatenno, K.; Zhang, G.; Kuramochi, E.; Shinya, A.; Notomi, M. Continuous-Wave Operation and 10-Gb/s Direct Modulation of InAsP/InP Sub-Wavelength Nanowire Laser on Silicon Photonic Crystal. *APL Photonics* **2017**, *2*, 046106.

(18) Tiwari, P.; Wen, P.; Caimi, D.; Mauthe, S.; Triviño, N. V.; Sousa, M.; Moselund, K. E. Scaling of Metal-Clad InP Nanodisk Lasers: Optical Performance and Thermal Effects. *Opt. Express* **2021**, *29*, 3915.

(19) Xu, C.; Hayenga, W. E.; Khajavikhan, M.; Likamwa, P. Measuring the Frequency Response of Optically Pumped Metal-Clad Nanolasers. *Opt. Express* **2019**, *27*, 21834.

(20) Hayenga, W. E.; Garcia-Gracia, H.; Hodaei, H.; Reimer, C.; Morandotti, R.; LiKamWa, P.; Khajavikhan, M. Second-Order Coherence Properties of Metallic Nanolasers. *Optica* **2016**, *3*, 1187.

(21) Ding, K.; Hill, M. T.; Liu, Z. C.; Yin, L. J.; van Veldhoven, P. J.; Ning, C. Z. Record Performance of Electrical Injection Sub-Wavelength Metallic-Cavity Semiconductor Lasers at Room Temperature. *Opt. Express* **2013**, *21*, 4728.

(22) Hill, M. T.; Oei, Y.-S.; Smalbrugge, B.; Zhu, Y.; de Vries, T.; van Veldhoven, P. J.; van Otten, F. W. M.; Eijkemans, T. J.; Turkiewicz, J. P.; de Waardt, H.; Geluk, E. J.; Kwon, S.-H.; Lee, Y.-H.; Nötzel, R.; Smit, M. K. Lasing in Metallic-Coated Nanocavities. *Nat. Photonics* **2007**, *1*, 589–594.

(23) Kreinberg, S.; Laiho, K.; Lohof, F.; Hayenga, W. E.; Holewa, P.; Gies, C.; Khajavikhan, M.; Reitzenstein, S. Thresholdless Transition to Coherent Emission at Telecom Wavelengths from Coaxial Nanolasers with Excitation Power Dependent β -Factors. *Laser Photon. Rev.* **2020**, *14*, 2000065.

(24) Lu, Y.-J.; Wang, C.-Y.; Kim, J.; Chen, H.-Y.; Lu, M.-Y.; Chen, Y.-C.; Chang, W.-H.; Chen, L.-J.; Stockman, M. I.; Shih, C.-K.; Gwo, S. All-Color Plasmonic Nanolasers with Ultralow Thresholds:

- Autotuning Mechanism for Single-Mode Lasing. *Nano Lett.* **2014**, *14*, 4381–4388.
- (25) Zhang, G.; Takiguchi, M.; Tateno, K.; Tawara, T.; Notomi, M.; Gotoh, H. Telecom-Band Lasing in Single InP/InAs Heterostructure Nanowires at Room Temperature. *Sci. Adv.* **2019**, *5*, No. eaat8896.
- (26) Mauthe, S.; Vico Trivino, N.; Baumgartner, Y.; Sousa, M.; Caimi, D.; Stoferle, T.; Schmid, H.; Moselund, K. E. InP-on-Si Optically Pumped Microdisk Lasers via Monolithic Growth and Wafer Bonding. *IEEE J. Sel. Top. Quantum Electron.* **2019**, *25*, 1–7.
- (27) Wirths, S.; Mayer, B. F.; Schmid, H.; Sousa, M.; Gooth, J.; Riel, H.; Moselund, K. E. Room-Temperature Lasing from Monolithically Integrated GaAs Microdisks on Silicon. *ACS Nano* **2018**, *12*, 2169–2175.
- (28) Shi, B.; Zhu, S.; Li, Q.; Wan, Y.; Hu, E. L.; Lau, K. M. Continuous-Wave Optically Pumped 1.55 Mm InAs/InAlGaAs Quantum Dot Microdisk Lasers Epitaxially Grown on Silicon. *ACS Photonics* **2017**, *4*, 204–210.
- (29) Yan, Z.; Han, Y.; Lin, L.; Xue, Y.; Ma, C.; Ng, W. K.; Wong, K. S.; Lau, K. M. A Monolithic InP/SOI Platform for Integrated Photonics. *Light Sci. Appl.* **2021**, *10*, 200.
- (30) Varshni, Y. P. Temperature Dependence of the Energy Gap in Semiconductors. *Physica* **1967**, *34*, 149–154.
- (31) Noh, W.; Dupré, M.; Ndao, A.; Kodigala, A.; Kanté, B. Self-Suspended Microdisk Lasers with Mode Selectivity by Manipulating the Spatial Symmetry of Whispering Gallery Modes. *ACS Photonics* **2019**, *6*, 389–394.
- (32) Bogdanov, A. A.; Mukhin, I. S.; Kryzhanovskaya, N. V.; Maximov, M. V.; Sadrieva, Z. F.; Kulagina, M. M.; Zadiranov, Y. M.; Lipovskii, A. A.; Moiseev, E. I.; Kudashova, Y. V.; Zhukov, A. E. Mode Selection in InAs Quantum Dot Microdisk Lasers Using Focused Ion Beam Technique. *Opt. Lett.* **2015**, *40*, 4022.
- (33) Moiseev, E. I.; Kryzhanovskaya, N.; Polubavkina, Y. S.; Maximov, M. V.; Kulagina, M. M.; Zadiranov, Y. M.; Lipovskii, A. A.; Mukhin, I. S.; Mozharov, A. M.; Komissarenko, F. E.; Sadrieva, Z. F.; Krasnok, A. E.; Bogdanov, A. A.; Lavrinenko, A. V.; Zhukov, A. E. Light Outcoupling from Quantum Dot-Based Microdisk Laser via Plasmonic Nanoantenna. *ACS Photonics* **2017**, *4*, 275–281.
- (34) Kryzhanovskaya, N.; Polubavkina, Y.; Moiseev, E.; Maximov, M.; Zhurikhina, V.; Scherbak, S.; Lipovskii, A.; Kulagina, M.; Zadiranov, Y.; Mukhin, I.; Komissarenko, F.; Bogdanov, A.; Krasnok, A.; Zhukov, A. Enhanced Light Outcoupling in Microdisk Lasers via Si Spherical Nanoantennas. *J. Appl. Phys.* **2018**, *124*, 163102.
- (35) Doleman, H. M.; Verhagen, E.; Koenderink, A. F. Antenna–Cavity Hybrids: Matching Polar Opposites for Purcell Enhancements at Any Linewidth. *ACS Photonics* **2016**, *3*, 1943–1951.
- (36) Doleman, H. M.; Dieleman, C. D.; Mennes, C.; Ehrler, B.; Koenderink, A. F. Observation of Cooperative Purcell Enhancements in Antenna–Cavity Hybrids. *ACS Nano* **2020**, *14*, 12027–12036.
- (37) Koenderink, A. F. Single-Photon Nanoantennas. *ACS Photonics* **2017**, *4*, 710–722.
- (38) Palstra, I. M.; Doleman, H. M.; Koenderink, A. F. Hybrid Cavity-Antenna Systems for Quantum Optics Outside the Cryostat? *Nanophotonics* **2019**, *8*, 1513–1531.
- (39) El-Sayed, M. A. Some Interesting Properties of Metals Confined in Time and Nanometer Space of Different Shapes. *Acc. Chem. Res.* **2001**, *34*, 257–264.
- (40) Wiley, B. J.; Chen, Y.; McLellan, J. M.; Xiong, Y.; Li, Z.-Y.; Ginger, D.; Xia, Y. Synthesis and Optical Properties of Silver Nanobars and Nanorice. *Nano Lett.* **2007**, *7*, 1032–1036.
- (41) Djorović, A.; Oldenburg, S. J.; Grand, J.; Le Ru, E. C. Extinction-to-Absorption Ratio for Sensitive Determination of the Size and Dielectric Function of Gold Nanoparticles. *ACS Nano* **2020**, *14*, 17597–17605.
- (42) Caimi, D.; Tiwari, P.; Sousa, M.; Moselund, K. E.; Zota, C. B. Heterogeneous Integration of III-V Materials by Direct Wafer Bonding for High-Performance Electronics and Optoelectronics. *IEEE Trans. Electron Devices* **2021**, *68*, 3149–3156.
- (43) Liao, J.; Ji, L.; Zhang, J.; Gao, N.; Li, P.; Huang, K.; Yu, E. T.; Kang, J. Influence of the Substrate to the LSP Coupling Wavelength and Strength. *Nanoscale Res. Lett.* **2018**, *13*, 280.
- (44) Castro-Lopez, M.; de Sousa, N.; Garcia-Martin, A.; Gardes, F. Y.; Sapienza, R. Scattering of a Plasmonic Nanoantenna Embedded in a Silicon Waveguide. *Opt. Express* **2015**, *23*, 28108.
- (45) Bennett, B. R.; Soref, R. A.; Del Alamo, J. A. Carrier-Induced Change in Refractive Index of InP, GaAs and InGaAsP. *IEEE J. Quantum Electron.* **1990**, *26*, 113–122.
- (46) Tatebayashi, J.; Kako, S.; Ho, J.; Ota, Y.; Iwamoto, S.; Arakawa, Y. Room-Temperature Lasing in a Single Nanowire with Quantum Dots. *Nat. Photonics* **2015**, *9*, 501–505.
- (47) Wang, Z.; Tian, B.; Pantouvaki, M.; Guo, W.; Absil, P.; Van Campenhout, J.; Merckling, C.; Van Thourhout, D. Room-Temperature InP Distributed Feedback Laser Array Directly Grown on Silicon. *Nat. Photonics* **2015**, *9*, 837.
- (48) Han, Y.; Ng, W. K.; Xue, Y.; Li, Q.; Wong, K. S.; Lau, K. M. Telecom InP/InGaAs Nanolaser Array Directly Grown on (001) Silicon-on-Insulator. *Opt. Lett.* **2019**, *44*, 767.
- (49) Salamin, Y.; Ma, P.; Baeuerle, B.; Emboras, A.; Fedoryshyn, Y.; Heni, W.; Cheng, B.; Josten, A.; Leuthold, J. 100 GHz Plasmonic Photodetector. *ACS Photonics* **2018**, *5*, 3291–3297.
- (50) Melikyan, A.; Alloatti, L.; Muslija, A.; Hillerkuss, D.; Schindler, P. C.; Li, J.; Palmer, R.; Korn, D.; Muehlbrandt, S.; Van Thourhout, D.; Chen, B.; Dinu, R.; Sommer, M.; Koos, C.; Kohl, M.; Freude, W.; Leuthold, J. High-Speed Plasmonic Phase Modulators. *Nat. Photonics* **2014**, *8*, 229–233.
- (51) Thomaschewski, M.; Zenin, V. A.; Wolff, C.; Bozhevolnyi, S. I. Plasmonic Monolithic Lithium Niobate Directional Coupler Switches. *Nat. Commun.* **2020**, *11*, 748.